ORIGINAL ARTICLE

Processability of high-strength aluminum 6182 series alloy via laser powder bed fusion (LPBF)

Kirstin Riener[1,2] · Tino Pfalz[1,3] · Florian Funcke[1,4] · Gerhard Leichtfried[2]

Abstract

The growing demand for more materials available for the LPBF-process, in particular high-strength aluminum alloys, is evident in the market. In the present work, a systematic investigation of the processability of aluminum 6182 series alloys, using LPBF, was carried out. For this purpose, the influence of process parameters, especially of enhanced preheating by heating the substrate plate during the LPBF process, on the microstructure of EN AW 6182 specimens was studied.

Experiments were conducted at different preheating temperatures always using the same d-optimal design-of-experiments, the laser power, scanning speed, hatch distance, and laser focus position being varied over a wide range.

It was found that the preheating temperature has the strongest impact on hot cracking. Higher temperatures result in a significantly reduced number of hot cracks in the microstructure. Moreover, an equiaxed microstructure of the specimens manufactured can be observed at preheating temperatures of 500 °C. In addition to the preheating temperature, the achievable part density is most strongly affected by the laser focus position and the laser power, whereas the hatch distance shows no discernible impact on the part density. Furthermore, neither the hatch distance nor the laser focus position shows any significant effect on hot cracking.

In combination with the optimal scanning parameters, crack-free parts with a fully equiaxed grain structure and densities > 99.0% can be manufactured via LPBF at a preheating temperature of 500 °C.

Keywords Additive manufacturing · Microstructure · Hot cracking · Density · AlSi1MgMn · 6000 series aluminum

Highlights

- Detailed studies about the processability of EN AW 6182 aluminum via LPBF were performed.
- With aluminum alloy EN AW 6182, the transition from columnar to equiaxed grains starts at a preheating temperature of 400 °C.
- Crack-free EN AW 6182 parts with an equiaxed microstructure and a density of 99.0% can be produced at a preheating temperature of 500 °C using LPBF.

✉ Kirstin Riener
  kirstin.riener@bmw.de

[1] BMW Group FIZ, Knorrstraße 147, 80788 Munich, Germany

[2] University of Innsbruck, Institute of Mechatronics, Materials Science, Technikerstraße 13, 6020 Innsbruck, Austria

[3] Dresden University of Technology, Institute of Materials Science, Helmholtzstraße 7, 01069 Dresden, Germany

[4] Technical University of Munich, Materials Engineering of Additive Manufacturing, 85748 Munich, Germany

1 Introduction

Additive manufacturing (AM) describes the layer-wise, successive build-up of parts. Laser powder bed fusion (LPBF) in particular enables the production of almost fully dense components with complex geometries by completely melting metal powder [1]. The above-mentioned advantages make the LPBF process perfectly suitable for fast production of individual parts and small series since tooling is not always required [2]. As a result of these characteristics, one of the main applications of the LPBF process is the manufacturing of functional prototypes. For this purpose, it is important to reproduce the properties of the future series part [3].

Of the high-strength wrought aluminum alloys, AlSi1MgMn or EN AW 6082 and AlSi1MgZr or EN AW 6182 are widely used for chassis parts and other components in the automotive industry due to their good weldability, corrosion resistance, and the possibility of heat treatment [4, 5].

When using LPBF, the most studied and processed aluminum alloys are the casting alloys AlSi12 and AlSi10Mg

[6–11]. Even if the mechanical properties of these two materials can be varied over a wide range by different heat treatments, it is not possible to duplicate the properties of wrought aluminum alloys, especially those of conventionally manufactured EN AW 6×82 / DIN EN 755-2 [7, 12–14].

In contrast to the above-mentioned casting alloys, which are already well understood in processing by LPBF, high-strength aluminum alloys have recently become part of the scientific focus, marking a new class of material and therefore creating new use cases for additively manufactured parts [15–24]. Latest studies have mainly focused on copper-containing materials like EN AW 6061 [15–17, 22, 24–26],as well as on alloys of the 7xxx series [18, 27] and the processing of 5xxx series aluminum alloyed with Sc or Zr, like Scalmalloy® [19, 20]. The main challenge for the 6xxx and 7xxx alloys is their susceptibility to hot cracking during the LPBF process. Hot cracking susceptibility of those alloys is attributed to the high-temperature interval between solidus and liquidus temperature because of their hypoeutectic composition [28]. This leads to the formation of long dendrites during solidification. As the temperature decreases and the solid phase content increases, liquid residual melt becomes trapped inside the interdendritic spaces. Upon solidification, volume contraction occurs due to the solid–liquid phase transition. The induced stresses are causing a separation of the liquid phase from the solid phase, which results in the formation of a crack [19].

Therefore, great efforts have been made to minimize this problem by preheating or by adding secondary particulates and elements with a known grain refining effect like TiB_2 or Zr [15–25, 27, 29, 30]. Zhou et al. [31] were able to produce crack-free samples of AA5083 alloy by modifying the prealloyed powder with 0.89 wt.% Zr. The suppression in crack formation was attributed to the grain refining effect of primary Al_3Zr particles, which formed at the melt pool boundary during solidification, as well as to the concomitant reduction in solidification range. This led to the formation of a distinct microstructure consisting of a band of small equiaxed grains at the melt pool boundary and columnar grains inside the melt pool. Zhou et al. proposed that the small equiaxed grains prevent cracks from propagating along grain boundaries due to their random orientation and high strength.

The aim of the present study is to provide correlations between process parameters in the LPBF-process and the properties of the processed material such as its microstructure, part density, and the occurrence of hot cracks for the 6182 alloy. Using a d-optimal design-of-experiment, the laser power, scanning speed, hatch distance, laser focus position, and substrate plate temperature were varied over a wide range. In order to take advantage of the positive influence on crack prevention of the grain refining element Zr, AlSi1MgZr (or EN AW 6182) was used in this study.

2 Material and methods

2.1 Material and its characterization

The powder used in this study was inert gas atomized by IMR Metal Powder Technologies GmbH and has a nominal particle size distribution of 20 – 63 μm, with an average powder particle size of 40 μm. For the sake of simplicity, it is named 6182 in this publication instead of EN AW 6182 or AlSi1MgZr.

The chemical composition of the powder was determined by inductively coupled plasma optical emission spectrometry (ICP-OES) on a 5100 ICP-OES from Agilent Technologies. Using carrier gas hot extraction with an ONH836 system from LECO, the content of O, N, and H was analyzed. The results are shown in Table 1.

The scanning electron microscope (SEM) Zeiss Supra 40VP from Carl Zeiss AG was used to gain a first impression of the particle shape and surface morphology. SEM micrographs are presented in Fig. 1 and show a mostly spherical powder with several elongated particles and only few satellite attachments on the particle surface.

2.2 LPBF process

All samples for examining the part density and the amount of hot cracks were produced on the LPBF machine AconityONE from Aconity GmbH, equipped with four Nd:YAG solid-state lasers with a maximum laser beam power of 700 W each. Nitrogen was used as shielding gas. The process parameters being used are listed in Table 2. Besides the temperature of the substrate plates, which will be referred to as the preheating temperature in the following text, the laser power P_L and scanning speed v_{scan}, hatch distance d_{hatch}, and laser focus position $shift_{focus}$ were varied over a wide range. In this study, a laser focus position of $shift_{focus} = 0.9$ mm

Table 1 Chemical composition of the processed 6182 powder

Element	Chemical composition (wt.-%)
Si	1.02
Mg	1.04
Mn	0.79
Fe	0.11
Cr, Cu, Ti, Zn	<0.10
Zr	0.18
Al	Bal
	Content (μg/g)
O	335
N	<10
H	24.4

Fig. 1 SEM micrographs of the used powder
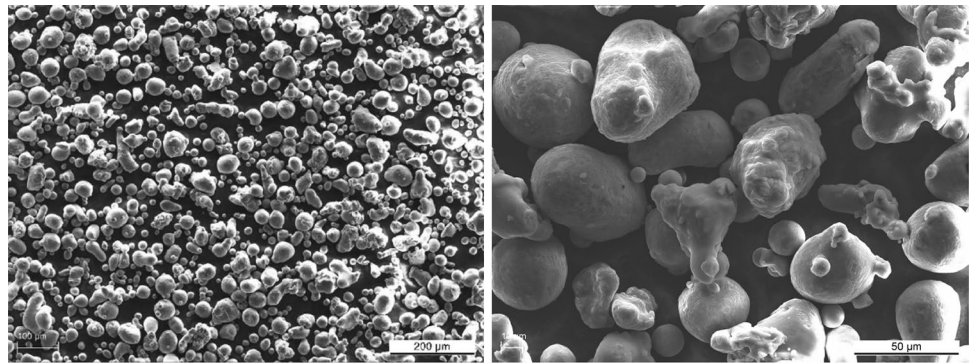
means that the laser beam is focused on the exposure plane with a laser beam diameter of 106 μm. At a laser focus position of $shift_{focus} = 6.9$ mm or $shift_{focus} = 10.0$ mm, the laser beam is defocused with a shift toward the divergent direction which results in a laser beam diameter of 154 μm (for a laser focus position of $shift_{focus} = 6.9$ mm). A laser focus position of $shift_{focus} = 10.0$ mm results in a laser beam diameter of 198 μm, respectively. The laser beam diameters were measured according to DIN EN ISO 11146 using a BeamWatch® AM from Ophir Optronics Solutions Ltd.

Cubes with dimensions of 10 mm × 10 mm × 16 mm were built by scanning the laser across the surface in stripes. The direction of scanning was rotated by 67° between successive powder layers and a nominal layer thickness t_{layer} of 50 μm was used.

Laser power P_L, powder layer thickness t_{layer}, scanning speed v_{scan}, and hatch distance d_{hatch} define the characteristic volumetric energy density E_V according to Eq. (1) [32, 33].

$$E_v = \frac{P_L}{t_{layer} * v_{scan} * d_{hatch}} \tag{1}$$

To characterize the effect of the various process parameters on the part properties, a design of experiments (DoE) was developed using Visual-XSel 15 from CRGRAPH GbR. A cubic model was chosen to represent nonlinear relationships. In order to minimize the number of experiments while maintaining a good evaluation capability, the setup of the DoE was d-optimal [34]. Additionally, three central points and several additional tests were added to the DoE to assure an adequate statistical validation. The resulting 50 parameter combinations were used to manufacture 50 samples in one build job per preheating temperature. An overview of the DoE parameter combinations can be seen in the Appendix.

2.3 Characterization of the LPBF parts

In order to determine the density, cross sections of the built cubes parallel to the z-axis were investigated using the light microscope DM 4000 M LD from Leica Microsystems GmbH. Images were taken over the entire ground and polished cross section of the cubes. Subsequently, the images were edited with the image post-processor ImageJ and were then separated into dense areas and voids by using a grayscale threshold of 0 to 150. Afterward, the ImageJ tool "Analyze Particles" was executed. This Plug-In analyzes objects in binary or thresholded images. By scanning the image, it outlines objects and measures them, then resumes the scanning procedure until it reaches the end of the image or selection. The total density is determined by the quotient of the dense area (total area minus area of objects/voids) and the total area. A minimum pore size of 2 pixels and a form factor of the pores to be analyzed of 0.2 to 1.0 were defined. Particles outside this range specified are ignored. By limiting the form factor, cracks or scratches can be excluded from the evaluation and thus the error can be minimized.

To evaluate the crack density, a section of the light microscope image was selected. Subsequently, all cracks are drawn by hand in red and a HSB stack was created. In a HSB stack, colors are displayed sorted according to hue, saturation, and brightness in different planes. This way, the previously marked hot cracks can be filtered out of the overall image. Afterward, the ImageJ Plug-In "Skeletonize" was used [35]. The Skeletonize-Plug-In identifies the centerlines

Table 2 Overview of the process parameters used for sample manufacturing

Preheating temperature (T /°C)	200 – 300 – 400 – 500
Laser power (P_L/W)	260 – 325 – 390 – 455 – 520 – 585 – 650
Scanning speed (v_{scan} / mm/sec)	800 – 1000 – 1200 – 1400 – 1600 – 1800 – 2000
Hatch distance (d_{hatch} /mm)	0.11 – 0.13 – 0.15
Laser focus position ($shift_{focus}$ /mm)	0.9 – 6.9 – 10.0

("skeleton") of objects by iteratively eroding their surface. That way, the marked cracks with a pre-defined width were converted into a 1-pixel thick skeleton. In order to analyze the skeletons length, the ImageJ Plug-In "AnalyzeSkeleton 2D/3D" was used [35]. This Plug-In tags all pixels, identifies all branches in the skeletonized image, and measures their length. For more details, see [35, 36]. The length of each branch $l_{crack;i}$ was added up to calculate the total crack length in the current cross section (Fig. 2). By dividing the total crack length with the area of the image section A, a characteristic and comparable value for the crack density $l_{crack;norm}$ in the section plane can be obtained according to Eq. (2).

$$l_{crack;norm} = \frac{\sum_{n=1}^{i} l_{crack;i}}{A} \tag{2}$$

$l_{crack;norm}$ = crack density or normalized crack length (1/mm)
$l_{crack;i}$ = length of a single crack (mm)
A = area of the image section (mm^2)

It is noteworthy that the crack density according to Eq. (2) is limited to comparing the overall crack length over a given area. The amount or individual crack lengths cannot be compared due to the normalization.

Two cubes were analyzed for each parameter combination to form the average value of the density and the crack density.

The analysis of the grain size and orientation was conducted using electron backscattered diffraction (EBSD). The measurements were performed on the Philips FEI XL 30 scanning electron microscope with an integrated INCA-Crystal EBSD system from Oxford Instruments. The lower resolution limit (or size of a single pixel) was 2.6 µm.

2.4 Statistical data analysis

The density and crack density values were evaluated by multiple regression using Visual X-Sel. Multiple regression assesses the influence of several independent parameters (preheating temperature, laser power, scanning speed,

hatch distance, and laser focus position) as well as interactions of these parameters on the dependent target value Y (density and crack density). The multiple regression model is described using the following general approach (Eq. 3):

$$Y = b_0 + b_1x_1 + b_2x_2 + ... + b_nx_n \tag{3}$$

Y = target value
b_0 = constant
b_n = regression coefficient
x_n = independent value

The regression coefficient b_n describes the mean change of the response variable (density or crack density) given a one-unit change in the predictor. To describe nonlinear relationships, the model can be extended by higher-order approaches (Eq. 4):

$$Y = b_0 + b_1x_1 + b_2x_1^2 + ... + b_nx_n \tag{4}$$

When interactions are present, the product of the interacting factors must be added to the model (Eq. 5):

$$Y = b_0 + b_1x_1 + b_2x_2 + b_{12} * x_1x_2 + ... + b_nx_n \tag{5}$$

The b_n values are calculated using the matrix form of the model equation (Eqs. 6, 7, and 8):

$$Y = Xb \tag{6}$$

$$Y = \begin{bmatrix} y_1 \\ y_2 \\ .. \\ y_n \end{bmatrix} X = \begin{bmatrix} 1 & x_{11} & x_{21} & .. & x_{11}^2 & x_{21}^2 & x_{11}x_{21} & x_{11}x_{31} \\ 1 & x_{12} & x_{22} & .. & .. & .. & ... & ... \\ .. & .. & .. & .. & ... & ... & ... & ... \\ 1 & x_{1n} & x_{2n} & .. & x_{1n}^2 & x_{2n}^2 & x_{1n}x_{2n} & x_{1n}x_{3n} \end{bmatrix} b = \begin{bmatrix} b_0 \\ b_1 \\ .. \\ b_n \end{bmatrix} \tag{7}$$

$$b = (X^TX)^{-1}X^Ty \tag{8}$$

An important characteristic value of the multiple regression model is the coefficient of determination R^2. Coefficients of determination closer to 1 mean that the model is more reliable in predicting the target value Y. R^2 is defined as the ratio of the regression sum of squares SS_{Reg} and the total sum of squares SS_{Total} (Eq. 9).

Fig. 2 ImageJ procedure for determining the crack density

Marking of the cracks   HSB-Stack; Skeletonize   Analyze skeleton
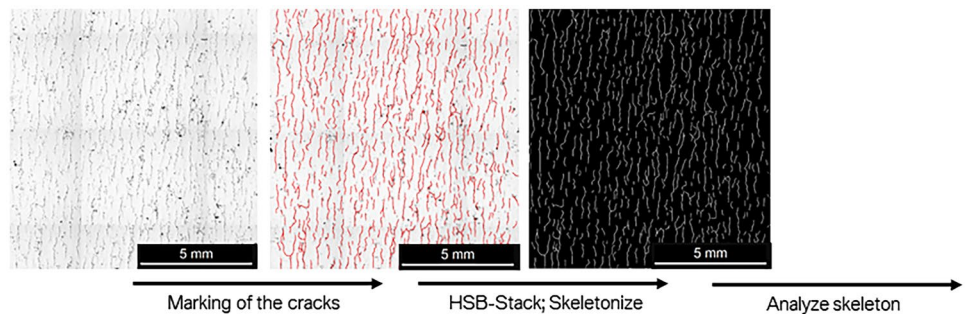
$$R^2 = \frac{SS_{Reg}}{SS_{Total}} \tag{9}$$

The p value was used to evaluate if an independent parameter has a significant influence on the target value. The significance level was set to 5%, meaning that parameters with a p value above 0.05 did not exhibit a significant influence on the target value [37, 38].

3 Results and discussion

3.1 Influence of scanning parameters and preheating on the LPBF part densies

Figure 3 shows the model graphic of the multiple regression of the density analysis. Only significant influencing variables with a p value of less than 0.05 are used. Scanning speed and hatch distance are not removed from the regression model despite higher p values, since both parameters are present in statistically significant interactions. This results in a coefficient of determination of $R^2 = 66.1\%$; thus, the relationships can only be partially explained. The interaction of laser power and scanning speed has the greatest influence on the density with $b_n = 3.255$. The smallest coefficient $b_n = 0.016$ is provided by the hatch distance.

The mathematical regression model is shown in a curve diagram (Fig. 4). The density is calculated using selected values for the influencing parameters (vertical red lines). The curves in the diagram describe how the target value would behave when changing the respective influencing variable, while keeping the other variables constant. The dotted, light gray lines describe the 95% confidence interval of the regression. Using the regression model, a density of 99.86% with a standard deviation of 0.72% is calculated

for the parameter combination indicated by the red lines. Experimentally, the part density was determined with 99.8%, which fits the regression model. However, the curves shown in Fig. 4 describe only partially the actual relationships, as indicated by the coefficient of determination. According to the regression model, relative part densities of over 100% could be achieved, which, however, is physically impossible and must be related to errors that occur during the execution or evaluation of the experiment. Probably a major error is due to cracks being misinterpreted as pores. Due to its weaknesses, the regression model is appropriate to describe relative relationships, but not to obtain concrete predictions for porosity values.

The regression coefficient of the preheating temperature $b_n = -0.48$ is illustrated in Fig. 5. With higher preheating temperatures, the length of the melt pool and the melt lifetime increase, thus facilitating the generation of hydrogen porosity [39]. The increase in porosity, when the preheating temperature is changed from 200 °C to 300 °C, is small while it is considerable when the temperature is increased from 400 °C to 500 °C. At 500 °C, in addition to the increased formation of hydrogen pores, the hydrogen dissolved in the lattice could also recombine into spherical pores again [40]. Moreover, a higher preheating temperature also leads to an increase in depth, width, and length of the melt pool, which may result in a collapse of the key-hole and hence could lead to a further increase of spherical porosity defects [41].

At 500 °C, some pores are several millimeters in size with an elongated extension in the building direction (Fig. 6). This effect can be attributed to Ostwald ripening. During the manufacturing process, mainly microscopic pores are initially formed. Due to the increased diffusion rate at 500 °C, a directed vacancy migration from smaller to larger pores occurs. This results in the growth of large pores and

Fig. 3 Regression coefficients b_n of the individual influencing parameters and interactions for the target value "density"
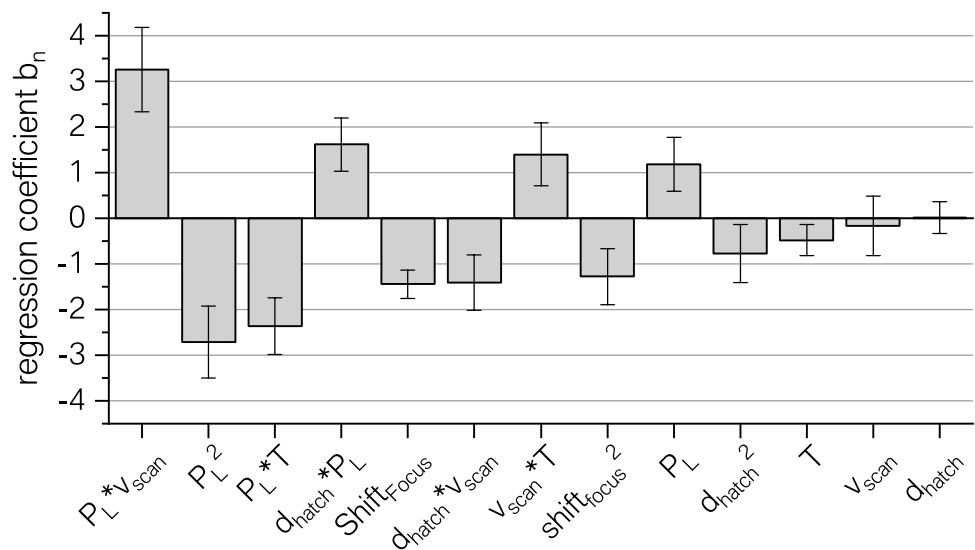
Fig. 4 Mathematical regression model. $T = 200\ °C$; $P_L = 455\ W$; $v_{scan} = 1400\ mm/sec$; $d_{hatch} = 0.13\ mm$, $shift_{focus} = 0.9\ mm$
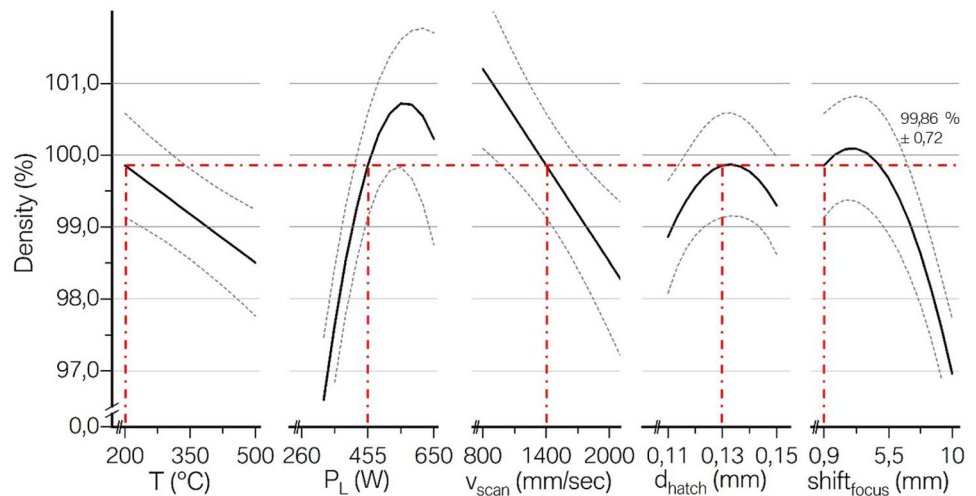
simultaneous annihilation of small ones. Thereby, the number of pores decreases while their size increases. Cracks, on the other hand, are not subject to Ostwald ripening, as they do not have curved surfaces and therefore do not act as a source or sink for vacancies [42, 43].

The influence of the laser power follows a quadratic relationship with $b_n = 1.18$. Toward lower laser powers, the density decreases. Lack-of-fusion pores can form because the melt does not show a sufficient coverage of the underlying layers. If the laser power exceeds an optimum, key-hole pores will occur [44, 45].

With $b_n = -0.18$, the part density is only slightly influenced by the scanning speed. This refers to an increase in key-hole porosity due to an increase in the instability of the vapor capillary in the melt pool. The scanning speed only shows larger influences on the part density in interaction with the laser power and the preheating temperature (Fig. 3).

The influence of the hatch distance is also small with $b_n = 0.17$. The quadratic relationship is in contradiction to the literature, which describes a decrease in density with

larger hatch distances [44]. One possible explanation for this observation might be that the interval in which the hatch distance was varied is comparatively small.

Between focus position and density, a quadratic relationship with a coefficient of $b_n = -1.45$ exists. At strong defocusing, the beam diameter increases, and the energy of the laser is distributed over a larger area. Consequently, the energy is too low to completely melt the powder particles or the solidified layers, which leads to an increased formation of lack-of-fusion pores (Fig. 7). Otherwise, the energy of the laser could become too high when focusing on a small area, which could lead to key-hole porosity [46, 47].

3.2 Interaction of scanning parameters and preheating regarding the part density

Scanning speed and hatch distance only show significant effects in interaction with the laser power. Figure 8 displays the corresponding interaction diagram. The focus position reveals no significant interaction with any parameter and is therefore not shown. Each pair of curves with

Fig. 5 Influence of the preheating temperature on the part density: $P_L = 455\ W$; $v_{scan} = 1400\ mm/sec$; $d_{hatch} = 0.13\ mm$, $shift_{focus} = 0.9\ mm$, $E_V = 50.0\ J/mm^3$

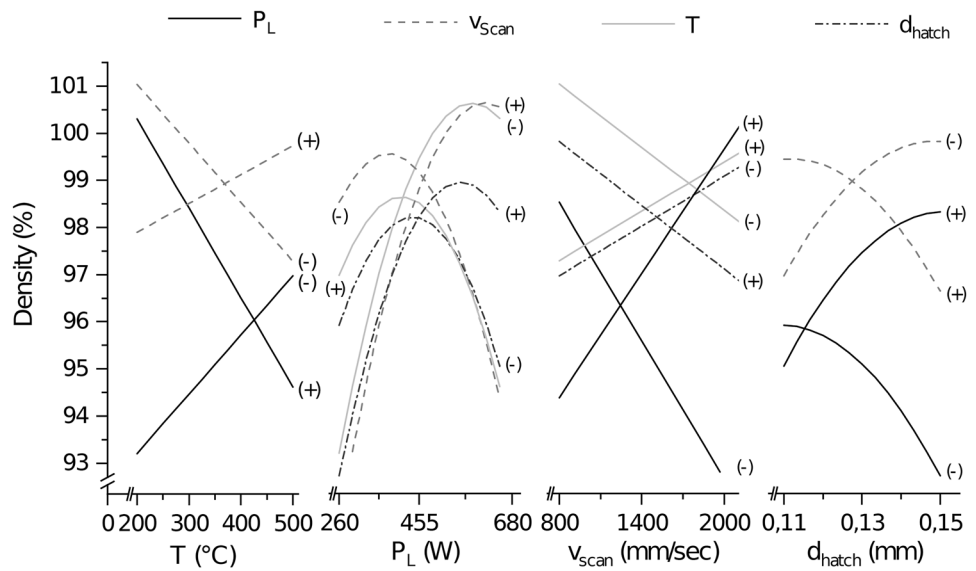While the part density decreases with increase in preheating temperature with the upper setting of the laser power, the curve with the upper setting of the scanning speed is exactly the opposite. It increases with higher laser power and decreases with higher scanning speeds. Therefore, the part density depends on the energy introduced at the set preheating temperature. The underlying reason is the reduction of the temperature gradient between the powder bed and the liquidus temperature of aluminum. At higher preheating temperatures, less energy is required to fuse the powder. As a result, the energy range at which the highest densities are achieved shifts to lower energies. If the energy input is not reduced at higher preheating temperatures, the surplus of energy in the system contributes to an increase in key-hole and hydrogen porosity.

The influence of the laser power on the density is determined by the scanning speed, preheating temperature, and the hatch distance, as well as by the thermophysical properties of the processed material. The scanning speed and hatch distance curves show the same course since they are both in the denominator of the volume energy density. Compared to the interaction of hatch distance and laser power, the interaction of scanning speed and laser power shows a greater influence on the achievable density. At lower temperature settings, the maximum density shifts to higher laser power. Moreover, the maximum achievable density is significantly higher at a lower temperature setting, due to the lower susceptibility to the formation of hydrogen and key-hole pores. As already described, the density tends to decrease with increase in preheating temperature.

The influence of the scanning speed on the density is influenced by the laser power, temperature, and hatch distance. Scanning speed and laser power have an influence on the interaction between hatch distance and density. As discussed earlier, all curves describe the same relationship between volume energy density and part density.

The following statements can be derived from the interaction diagrams. The scanning parameters laser power,

Fig. 6 Negative effects of the Ostwald ripening on the part density at preheating temperatures of 500 °C. $P_L = 520$ W; $v_{scan} = 1800$ mm/sec; $d_{hatch} = 0.13$ mm, shift$_{focus} = 10.0$ mm, density $= 94.0\%$

its encoding stands for the respective influencing variables. A curve marked with a (+) stands for the upper setting of the influencing variable, (-) for the lower setting. As already described for the regression model (Fig. 4), the relative part densities of over 100% can be related to deficiencies in data processing and evaluation.

Generally, the same linear and quadratic dependencies of the influencing parameters on the density can be seen in Fig. 4. However, the position and direction of the graphs change depending on the setting of the interacting variable. Laser power and scanning speed show an influence on the relationship between preheating and part density. This results from the volume energy density E_v (Eq. 1).

Fig. 7 Influence of the laser focus position on the density. $P_L = 455$ W; $v_{scan} = 1600$ mm/ sec; $d_{hatch} = 0.15$ mm; $T = 200$ °C

Fig. 8 Interaction plot for the target value part density

scanning speed, and hatch distance show strong interactions and can be described by the volume energy density. There is an optimal volume energy, which leads to the highest part densities. However, this energy is not absolute and describes a processing window, which depends in particular on the set preheating temperature and must be adapted to it. At higher temperatures, less energy is required to achieve maximum densities.

3.3 Influence of scanning parameters and preheating temperature on the crack density

Figure 9 shows the multiple regression of the crack density. The regression coefficients b_n range from a maximum of 0.6 for temperature to the power of three to a minimum of 0.06 for the focus shift. The p values are less than 0.05 for all significant coefficients. No significant interdependencies were found in the model, which results in a good fit with a coefficient of determination of 93.7%

The regression model postulates a crack density of $(2.33 + -0.07)$ mm^{-1} as shown in Fig. 10. Experimentally, the crack density was determined with 2.36 mm^{-1}, which fits the regression values. The hatch distance d_{hatch} exhibited no significant influence on the model and was therefore disregarded.

The preheating temperature with $b_n = 0.6$ shows the greatest influence on the crack density. With increase in temperature, the crack density significantly decreases, as Fig. 11 displays. At 500 °C, it was possible to produce crack-free samples due to the decreased temperature difference between the melt pool and the surrounding material, and the accompanying reduced solidification velocity. A longer time to solidification allows a better refill of the interdendritic spacing with the residual liquid metal to compensate for the volume contraction while cooling. This reduces hot cracking

Fig. 9 Regression coefficients b_n of the individual influencing parameters for the target value "crack density"
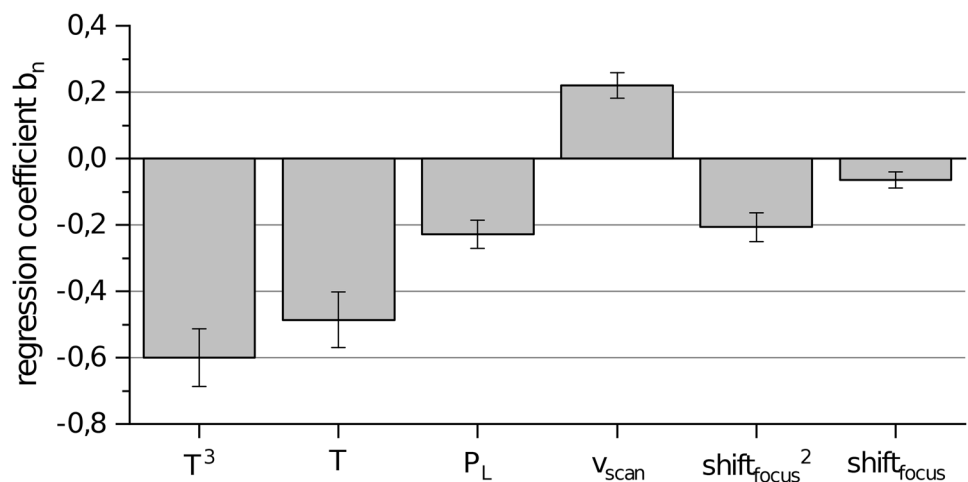
Fig. 10 Mathematical regression model. T = 200 °C; P_L = 455 W; v_{scan} = 1400 mm/sec; d_{hatch} = 0.13 mm, $shift_{focus}$ = 0.9 mm
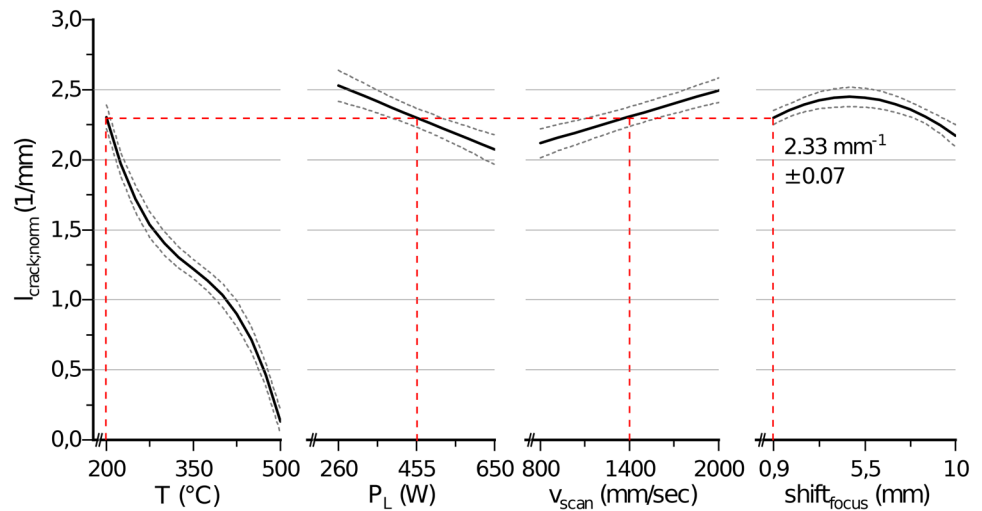
for most variations in laser parameters. However, in addition to avoiding hot cracks, porosity increases significantly at a preheating temperature of 500 °C (Fig. 11). The underlying phenomena are discussed in Sect. 3.1.

In addition to the preheating temperature, the laser scanning parameters determine whether hot cracks are formed.

In the presented results, the parameters "laser power P_L" and "laser scanning speed v_{scan}" determine the volume energy density E_v according to Eq. (1). Both parameters show a linear relationship to the crack density with a similar regression coefficient $|b_n|$ = 0.2 (Figs. 9 and 10). Higher energy input is achieved by both lower scanning speeds and higher laser power; decreased energy input is accomplished vice versa.

Increasing the laser power reduces the crack density by forming a hotter and less viscous melt bath, which leads to a better refill of the interdendritic spaces and thus compensates the volume contraction more effectively during cooling. Similarly, reducing the scanning speed decreases the crack density, since both the cooling and solidification rates per volume are decreased.

The focus shift shows a quadratic model with b_n = −0.21 and a maximum around $shift_{focus}$ = 5.5 mm. A focus shift parameter, set to $shift_{focus}$ = 0.9, results in small melt pools with low melt volumes as well as high-temperature gradients and cooling rates. This in turn leads to a finer microstructure with smaller grains [48], which can suppress the formation of hot cracks. Conversely, focus shift parameters set to $shift_{focus}$ = 10.0, result in larger melt pools with lower local temperature gradients and cooling rates. Thus, it enables the melt to fill the interdendritic spaces, which can also minimize the formation of hot cracks. The maximum crack density is around $shift_{focus}$ = 5.5. It can be assumed that larger melt pools and intermediate temperature gradients result in an unfavorable combination of a coarser microstructure and less time for the melt to fill the interdendritic spaces. Consequently, the susceptibility for hot cracks could be enhanced.

Figure 12 shows the hot cracking in consideration of the volume energy density. Increased energy densities reduce the normalized crack density, as, for example, at E_v = 54.17 J/mm³ the crack density is roughly three times less than at E_v = 36.93 J/mm³.
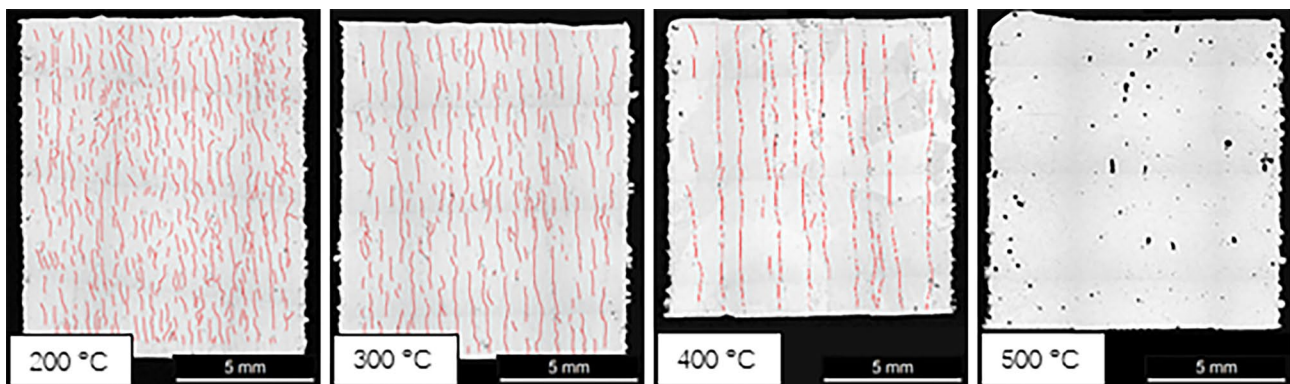
Fig. 11 Influence of the preheating temperature on the crack density. P_L = 455 W; v_{Scan} = 1400 mm/sec; d_{hatch} = 0.13 mm; $shift_{focus}$ = 0.9 mm

3.4 Influence of preheating on grain size and orientation in the LPBF parts

EBSD maps are shown in Figs. 14, 15, 16, and 17. All investigated specimens were manufactured with the same laser parameters $P_L = 455$ W; $v_{scan} = 1400$ mm/sec; $d_{hatch} = 0.13$ mm; $shift_{focus} = 0.9$ mm. Only the preheating temperature was varied. For each analyzed sample, the mappings of the grain orientation in normal direction (perpendicular to building direction) and transverse direction (parallel to building direction) are compared in order to underline the texture along the building direction (compare Fig. 13).

EBSD orientation mappings of the sample manufactured at a preheating temperature of 200 °C are shown in Fig. 14. The average grain size, expressed as the equivalent circular diameter (ECD), is determined as 33.72 μm. A noticeable change in orientation, occurring in some grains, indicates a very high defect or dislocation density. In the transverse direction, which represents the orientation in building direction, the grains are mostly oriented in [001] direction. Black areas in the EBSD mappings can be assigned to pores, hot cracks, and intermetallic phases and are primarily located at grain boundaries. This observation supports the assumption that the hot cracks are initiated by the volume contraction of the liquid residual melt that becomes trapped inside interdendritic spaces and the accompanying induced stresses.

At a preheating temperature of 300 °C, a more pronounced texture in the transverse direction is revealed (Fig. 15). This can be seen in the pole figure, which shows an increase in {100} reflections in the transverse direction compared to Fig. 14. In some grains, a change of orientation takes place again. The determined average grain size is
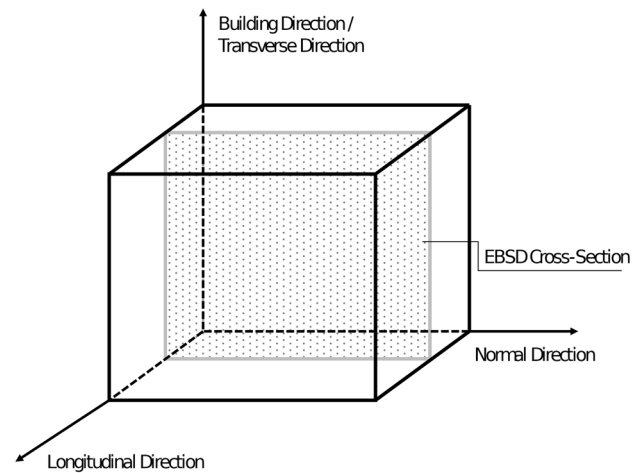
Fig. 13 Illustration of mapping directions for EBSD specimens

ECD = 27.15 μm. The grains show a columnar structure in which all grains are oriented along the building direction (or transverse direction) in [001] direction.

The most significant texture in building direction occurs in the sample manufactured at 400 °C (Fig. 16). Nearly all grains in the transverse direction are oriented along the [001] direction. The average grain size ECD = 25.35 μm.

In contrast to the other samples, the samples manufactured at 500 °C show a fully equiaxed grain structure without a pronounced texture (Fig. 17) and a mean grain size of ECD = 19.46 μm.

The texture becomes more pronounced with increase in preheating temperature, with a maximum for the sample manufactured at 400 °C. In this case, nearly all grains are oriented in [001] direction (parallel to the building direction), which is the direction of the preferred growth in the fcc crystal system.

| 36,93 J/mm³ | 42,21 J/mm³ | 50,00 J/mm³ | 54,17 J/mm³ |
| (a) | (b) | (c) | (d) |
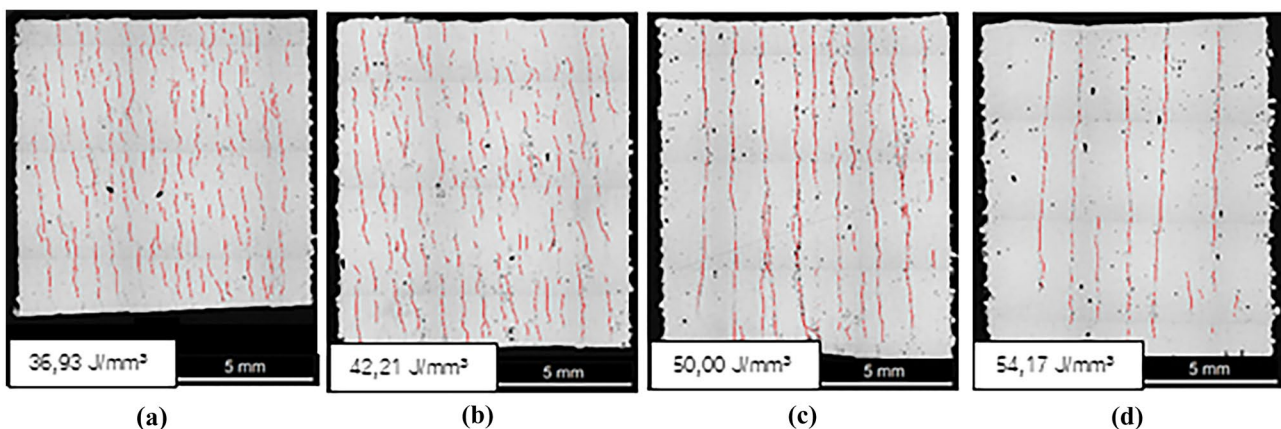
Fig. 12 Influence of the volume energy density; alloy EN AW 6182; T = 400 °C. (**a**) PL = 325 W; vScan = 1600 mm/sec; dhatch = 0.11 mm, shiftfocus = 0.9 mm, lcrack = 1.38 1/mm. (**b**) PL = 325 W; vScan = 1400 mm/sec; dhatch = 0.11 mm, shiftfo- cus = 0.9 mm, lcrack = 1.13 1/mm. (**c**) PL = 455 W; vScan = 1400 mm/ sec; dhatch = 0.13 mm, shiftfocus = 0.9 mm, lcrack = 1.05 1/mm (**d**) PL = 650 W; vScan = 1600 mm/sec; dhatch = 0.15 mm, shiftfo- cus = 0.9 mm, lcrack = 0.55 1/mm
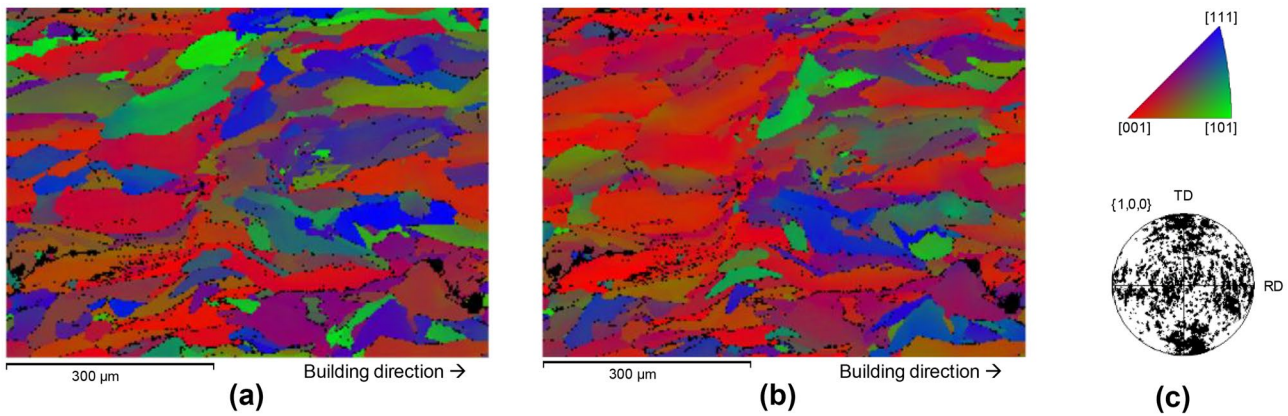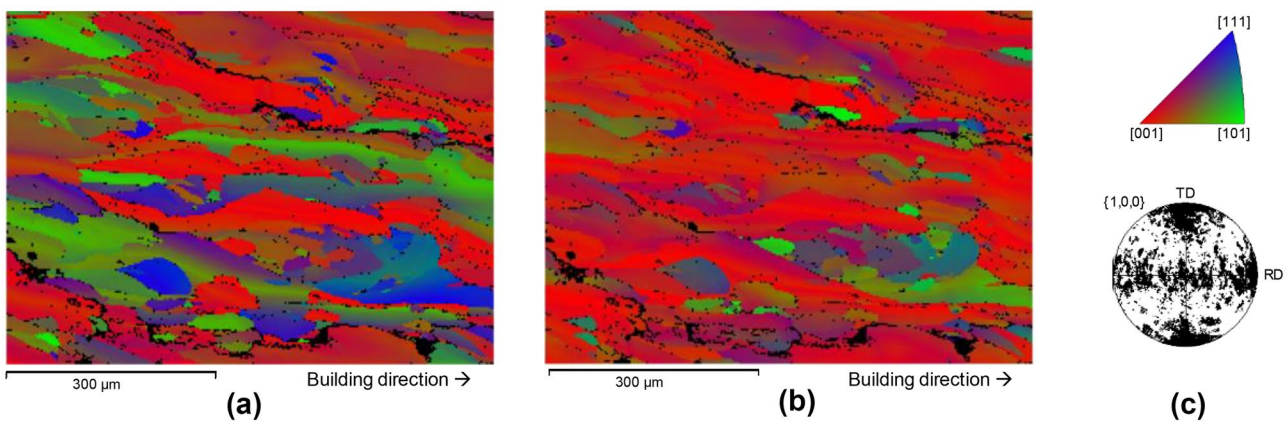
Fig. 14 EBSD micrograph. Orientation mapping in (**a**) normal, (**b**) transverse direction of the same cross section, (**c**) pole figure. T = 200 °C

Due to the heat flow directed against the building direction, a columnar structure with grains elongated in the building direction is formed. The increase in the number of grains oriented in [001] direction with increase in preheating temperature can be attributed to the decrease in cooling speed, which reduces the solidification speed. Thus, favorably oriented grains, i.e., grains oriented in [001] direction, exhibit a higher growth rate and can prevail over other less favorably oriented grains. Consequently, the grains of the 400 °C sample show the greatest expansion in the direction of growth. In contrast, due to the high solidification rates, the influence of the grain orientation on the growth rate is suppressed at lower preheating temperatures, which also enables grains with a less favorable crystallographic orientation to grow.

The characteristic, lens-shaped microstructure of LPBF parts made from aluminum cast alloys [49] does not occur at any preheating temperature. For the samples with preheating temperatures of 200 °C, 300 °C, and 400 °C, the grains developed in the building direction show heights up to 600 μm, which is higher than 10 single nominal powder layers. Therefore, it can be concluded that solidification mostly takes place epitaxially without the formation of new nuclei. Significant differences in the microstructure occur when the specimens were manufactured at a preheating temperature of 500 °C. A fully equiaxed microstructure without a pronounced texture evolves. According to [50], this can be attributed to the smaller temperature gradient due to the higher preheating temperature. As a result, the LPBF typical microstructure with columnar grains disappears and a globular microstructure with significantly smaller, equiaxed grains develops. Initial signs of equiaxial solidification can already be observed in the 400 °C sample. Between the elongated grains oriented in [001] direction, smaller globular grains can be observed.

Fig. 15 EBSD micrograph. Orientation mapping in (**a**) normal, (**b**) transverse direction of the same cross section, (**c**) pole figure. T = 300 °C
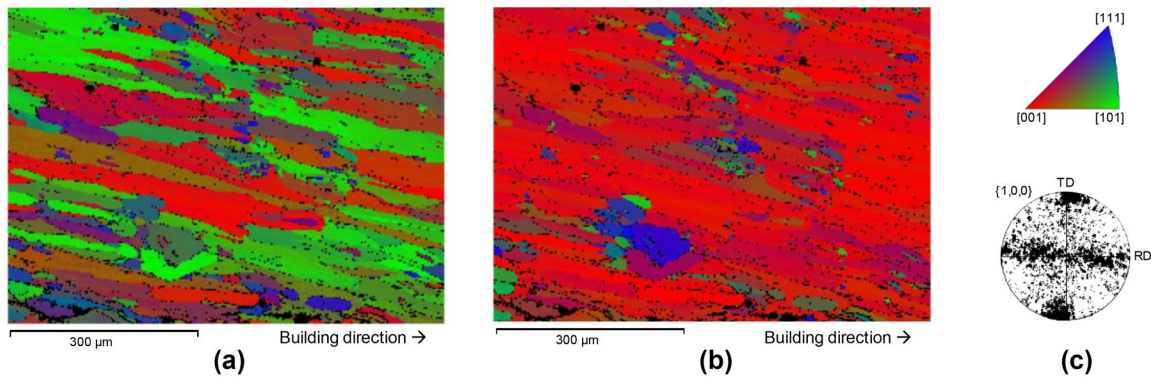
Fig. 16 EBSD micrograph. Orientation mapping in (**a**) normal, (**b**) transverse direction of the same cross section, (**c**) pole figure. T = 400 °C
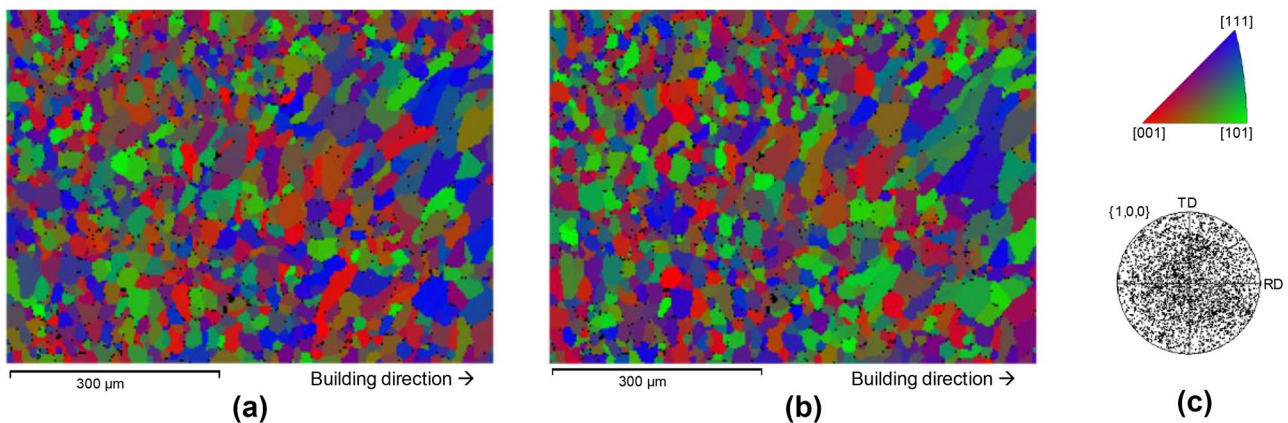
Fig. 17 EBSD micrograph. Orientation mapping in (**a**) normal, (**b**) transverse direction of the same cross section, (**c**) pole figure. T = 500 °C

4 Conclusion

Both increased preheating and increased volume energy density lead to less hot cracks in the microstructure. These effects can be attributed to a lower viscosity of the melt pool at higher temperatures. By increasing the preheating temperature to 500 °C, crack-free specimens with a maximum density of 99.0% can be produced. Independent of the laser parameters, it was not possible in this study to produce crack-free specimens with a preheating temperature below 500 °C. A further interesting aspect of the 500 °C samples is their fully equiaxed grain structure, which can be attributed to the lower temperature gradient in the melt pool due to the higher preheating temperature.

Considering these findings, two mechanisms that could suppress the formation of cracks are possible. First, the reduced solidification velocity due to the decreased temperature difference between melt pool and surrounding material allows a better refill of the interdendritic spacing with the residual liquid metal. Second, the grain refinement due to

fully equiaxed grain structure eliminates the formation of long liquid channels along the large columnar grain boundaries during solidification, and thus reduces the solidification cracks along the build direction.

The part density decreases as the preheating temperature increases. As a result of the Ostwald ripening, the pores coalesce under high temperatures and can form defects with a size of several millimeters. The influence of the laser parameters on the density can be described by the volume energy density. Within a certain energy range, highest densities > 99.5% can be reached. However, this range depends on the preheating temperature. At higher temperatures, the energy range at which maximum densities can be achieved shifts to lower energies. Adjusting the energy density and the individual scanning parameters to the increased platform temperature is the biggest lever in optimizing the part density.

The intended avoidance of hot cracking due to the grain refining effect of zirconium cannot be observed. Considering appropriate literature, the zirconium content of 0.18%

of alloy 6182 may be too low to positively influence the hot cracking behavior. Another explanation might be that the high cooling rates in the process may suppress the precipitation of the grain refining Al_3Zr phase and thus impede the grain refining effect of Zr [31, 51]. It can therefore be assumed that the Zr content must exceed a minimum and higher Zr contents might be necessary to achieve the desired grain refining effect and to suppress crack formation in the AlSi1Mg alloy.

Appendix

DoE for all examined material to preheating temperature combinations. All 50 specimens were manufactured at each preheating temperature

Nr°	Laser power (W)	Scanning speed (mm/sec)	Hatch distance (mm)	Laser focus position (mm)	Volume-based energy density [J/mm^3]
1	455	1400	0.13	0.9	50.00
2	390	1800	0.11	0.9	39.39
3	390	1000	0.11	10	70.91
4	650	1400	0.15	0.9	61.90
5	650	1400	0.15	6.9	61.90
6	455	1200	0.13	6.9	58.33
7	390	1400	0.13	6.9	42.86
8	455	1000	0.15	0.9	60.67
9	520	1000	0.15	10	69.33
10	325	1400	0.15	6.9	30.95
11	455	1600	0.15	0.9	37.92
12	325	1400	0.15	10	30.95
13	260	1400	0.11	6.9	33.77
14	520	1400	0.11	0.9	67.53
15	260	800	0.15	0.9	43.33
16	455	1600	0.11	6.9	51.70
17	325	1000	0.15	10	43.33
18	585	1800	0.11	0.9	59.09
19	585	1600	0.13	10	56.25
20	325	1400	0.11	0.9	42.21
21	325	1600	0.11	0.9	36.93
22	325	1800	0.13	6.9	27.78
23	260	1200	0.11	10	39.39
24	390	1600	0.13	0.9	37.50
25	455	1400	0.15	0.9	43.33
26	260	2000	0.11	10	23.64
27	455	1600	0.15	6.9	37.92
28	455	2000	0.11	6.9	41.36
29	585	1400	0.13	6.9	64.29
30	260	1800	0.15	6.9	19.26
31	585	2000	0.15	6.9	39.00
32	455	1600	0.11	10	51.70
33	585	2200	0.11	6.9	48.35
34	390	800	0.11	6.9	88.64
35	455	1000	0.15	6.9	60.67
36	325	1200	0.11	0.9	49.24
37	520	1800	0.15	10	38.52
38	585	2000	0.15	0.9	39.00
39	520	1800	0.13	10	44.44
40	520	2000	0.11	0.9	47.27
41	650	2200	0.11	10	53.72
42	455	1400	0.11	10	59.09
43	390	1400	0.15	6.9	37.14
44	455	2000	0.11	0.9	41.36
45	260	2000	0.15	0.9	17.33
46	390	1800	0.15	10	28.89
47	520	1200	0.15	10	57.78
48	455	800	0.13	10	87.50
49	455	1400	0.13	0.9	50.00
50	455	1400	0.13	0.9	50.00

Declarations

References

1. Oliveira JP, LaLonde AD, Ma J (2020) Processing parameters in laser powder bed fusion metal additive manufacturing. Mater Des 193:108762. https://doi.org/10.1016/j.matdes.2020.108762

2. Bremen S, Meiners W, Diatlov A (2012) Selective laser melting. Laser Technik J 9:33–38. https://doi.org/10.1002/latj.201290018

3. DebRoy T, Wei HL, Zuback JS et al (2018) Additive manufacturing of metallic components – process, structure and properties. Prog Mater Sci 92:112–224. https://doi.org/10.1016/j.pmatsci.2017.10.001

4. Benedyk JC (2010) Aluminum alloys for lightweight automotive structures. In: Materials, Design and Manufacturing for Lightweight Vehicles. Elsevier, pp 79–113

5. Polmear I, StJohn D, Nie J-F, Qian M (2017) Wrought aluminium alloys. In: Light Alloys. Elsevier, pp 157–263

6. Wei P, Wei Z, Chen Z et al (2017) The AlSi10Mg samples produced by selective laser melting: single track, densification, microstructure and mechanical behavior. Appl Surf Sci 408:38–50. https://doi.org/10.1016/j.apsusc.2017.02.215

7. Aboulkhair NT, Maskery I, Tuck C et al (2016) The microstructure and mechanical properties of selectively laser melted AlSi10Mg: The effect of a conventional T6-like heat treatment. Mater Sci Eng, A 667:139–146. https://doi.org/10.1016/j.msea.2016.04.092

8. Read N, Wang W, Essa K, Attallah MM (2015) Selective laser melting of AlSi10Mg alloy: Process optimisation and mechanical properties development. Mater Des 1980–2015(65):417–424. https://doi.org/10.1016/j.matdes.2014.09.044

9. Kempen K, Thijs L, Van Humbeeck J, Kruth J-P (2015) Processing AlSi10Mg by selective laser melting: Parameter optimisation and material characterisation. Mater Sci Technol 31:917–923. https://doi.org/10.1179/1743284714Y.0000000702

10. Li XP, Wang XJ, Saunders M et al (2015) A selective laser melting and solution heat treatment refined Al–12Si alloy with a controllable ultrafine eutectic microstructure and 25% tensile ductility. Acta Mater 95:74–82. https://doi.org/10.1016/j.actamat.2015.05.017

11. Riener K, Oswald S, Winkler M, Leichtfried GJ (2021) Influence of storage conditions and reconditioning of AlSi10Mg powder on the quality of parts produced by laser powder bed fusion (LPBF). Addit Manuf 39. https://doi.org/10.1016/j.addma.2021.101896

12. Fousová M, Dvorský D, Michalcová A, Vojtěch D (2018) Changes in the microstructure and mechanical properties of additively manufactured AlSi10Mg alloy after exposure to elevated temperatures. Mater Charact 137:119–126. https://doi.org/10.1016/j.matchar.2018.01.028

13. Li W, Li S, Liu J et al (2016) Effect of heat treatment on AlSi10Mg alloy fabricated by selective laser melting: Microstructure evolution, mechanical properties and fracture mechanism. Mater Sci Eng, A 663:116–125. https://doi.org/10.1016/j.msea.2016.03.088

14. Prashanth KG, Scudino S, Klauss HJ et al (2014) Microstructure and mechanical properties of Al–12Si produced by selective laser melting: Effect of heat treatment. Mater Sci Eng, A 590:153–160. https://doi.org/10.1016/j.msea.2013.10.023

15. Zhang H, Zhu H, Qi T et al (2016) Selective laser melting of high strength Al-Cu-Mg alloys: Processing, microstructure and mechanical properties. Mater Sci Eng, A 656:47–54. https://doi.org/10.1016/j.msea.2015.12.101

16. Uddin SZ, Murr LE, Terrazas CA et al (2018) Processing and characterization of crack-free aluminum 6061 using high-temperature heating in laser powder bed fusion additive manufacturing. Addit Manuf 22:405–415. https://doi.org/10.1016/j.addma.2018.05.047

17. Loh LE, Chua CK, Yeong WY et al (2015) Numerical investigation and an effective modelling on the Selective Laser Melting (SLM) process with aluminium alloy 6061. Int J Heat Mass Transf 80:288–300. https://doi.org/10.1016/j.ijheatmasstransfer.2014.09.014

18. Kaufmann N, Imran M, Wischeropp TM et al (2016) Influence of process parameters on the quality of aluminium alloy EN AW 7075 using Selective Laser Melting (SLM). Phys Procedia 83:918–926. https://doi.org/10.1016/j.phpro.2016.08.096

19. Martin JH, Yahata BD, Hundley JM et al (2017) 3D printing of high-strength aluminium alloys. Nature 549:365–369. https://doi.org/10.1038/nature23894

20. Awd M, Tenkamp J, Hirtler M et al (2017) Comparison of microstructure and mechanical properties of Scalmalloy® produced by selective laser melting and laser metal deposition. Materials 11:17. https://doi.org/10.3390/ma11010017

21. Li R, Wang M, Yuan T et al (2017) Selective laser melting of a novel Sc and Zr modified Al-6.2 Mg alloy: Processing, microstructure, and properties. Powder Technol 319:117–128. https://doi.org/10.1016/j.powtec.2017.06.050

22. Zhang H, Zhu H, Nie X et al (2017) Effect of Zirconium addition on crack, microstructure and mechanical behavior of selective laser melted Al-Cu-Mg alloy. Scripta Mater 134:6–10. https://doi.org/10.1016/j.scriptamat.2017.02.036

23. Nie X, Zhang H, Zhu H et al (2018) Effect of Zr content on formability, microstructure and mechanical properties of selective laser melted Zr modified Al-4.24Cu-1.97Mg-0.56Mn alloys. J Alloy Compd 764:977–986. https://doi.org/10.1016/j.jallcom.2018.06.032

24. Mair P, Kaserer L, Braun J et al (2021) Microstructure and mechanical properties of a TiB2-modified Al–Cu alloy processed by laser powder-bed fusion. Mater Sci Eng A 799:140209. https://doi.org/10.1016/j.msea.2020.140209

25. Carluccio D, Bermingham MJ, Zhang Y et al (2018) Grain refinement of laser remelted Al-7Si and 6061 aluminium alloys with Tibor® and scandium additions. J Manuf Process 35:715–720. https://doi.org/10.1016/j.jmapro.2018.08.030

26. Waller D, Polizzi A, Iten J (2019) Feasibility study of additively manufactured Al-6061 RAM2 parts for aerospace applications. In: AIAA Scitech 2019 Forum. American Institute of Aeronautics and Astronautics, Reston, Virginia

27. Jiang B, Zhenglong L, Xi C et al (2019) Microstructure and mechanical properties of TiB2-reinforced 7075 aluminum matrix composites fabricated by laser melting deposition. Ceram Int 45:5680–5692. https://doi.org/10.1016/j.ceramint.2018.12.033

28. Stopyra W, Gruber K, Smolina I et al (2020) Laser powder bed fusion of AA7075 alloy: Influence of process parameters on porosity and hot cracking. Addit Manuf 35:101270. https://doi.org/10.1016/j.addma.2020.101270

29. Wang P, Gammer C, Brenne F et al (2018) A heat treatable TiB2/Al-3.5Cu-1.5Mg-1Si composite fabricated by selective laser melting: Microstructure, heat treatment and mechanical properties. Compos B Eng 147:162–168. https://doi.org/10.1016/j.compositesb.2018.04.026

30. Zhou SY, Su Y, Wang H et al (2020) Selective laser melting additive manufacturing of 7xxx series Al-Zn-Mg-Cu alloy: Cracking elimination by co-incorporation of Si and TiB2. Addit Manuf 36:101458. https://doi.org/10.1016/j.addma.2020.101458

31. Zhou L, Hyer H, Park S et al (2019) Microstructure and mechanical properties of Zr-modified aluminum alloy 5083 manufactured by laser powder bed fusion. Addit Manuf 28:485–496. https://doi.org/10.1016/j.addma.2019.05.027

32. Mishurova T, Artzt K, Haubrich J et al (2019) New aspects about the search for the most relevant parameters optimizing SLM materials. Addit Manuf 25:325–334. https://doi.org/10.1016/j.addma.2018.11.023

33. Ghayoor M, Lee K, He Y et al (2020) Selective laser melting of 304L stainless steel: Role of volumetric energy density on the microstructure, texture and mechanical properties. Addit Manuf 32:101011. https://doi.org/10.1016/j.addma.2019.101011

34. de Aguiar PF, Bourguignon B, Khots MS et al (1995) D-optimal designs. Chemom Intell Lab Syst 30:199–210. https://doi.org/10.1016/0169-7439(94)00076-X

35. Arganda-Carreras I, Fernandez-Gonzalez R, Munoz-Barrutia A, Ortiz-De-Solorzano C (2010) 3D reconstruction of histological sections: Application to mammary gland tissue. Microsc Res Tech 73:1019–1029

36. Polder G, Hovens HLE, Zweers AJ (2010) Measuring shoot length of submerged aquatic plants using graph analysis. In: Proceedings of the ImageJ User and Developer Conference. Luxembourg, pp 172–177

37. Urban D, Mayerl J (2018) Angewandte Regressionsanalyse: Theorie, Technik und Praxis. Springer Fachmedien, Wiesbaden

38. CRGARPH (2016) https://crgraph.de/wp-content/uploads/2017/03/MultipleRegression.pdf

39. Sola A, Nouri A (2019) Microstructural porosity in additive manufacturing: The formation and detection of pores in metal parts fabricated by powder bed fusion. J Adv Manuf Process 1. https://doi.org/10.1002/amp2.10021

40. Weingarten C, Buchbinder D, Pirch N et al (2015) Formation and reduction of hydrogen porosity during selective laser melting of AlSi10Mg. J Mater Process Technol 221:112–120. https://doi.org/10.1016/j.jmatprotec.2015.02.013

41. Chen Q, Zhao Y, Strayer S et al (2020) Elucidating the effect of preheating temperature on melt pool morphology variation in Inconel 718 laser powder bed fusion via simulation and experiment. Addit Manuf 101642. https://doi.org/10.1016/j.addma.2020.101642

42. Lifshitz IM, Slyozov VV (1961) The kinetics of precipitation from supersaturated solid solutions. J Phys Chem Solids 19:35–50. https://doi.org/10.1016/0022-3697(61)90054-3

43. Wagner C (1961) Theorie der Alterung von Niederschlägen durch Umlösen (Ostwald-Reifung). Zeitschrift für Elektrochemie 65:581–591

44. Aboulkhair NT, Everitt NM, Ashcroft I, Tuck C (2014) Reducing porosity in AlSi10Mg parts processed by selective laser melting. Addit Manuf 1–4:77–86. https://doi.org/10.1016/j.addma.2014.08.001

45. Buchbinder D, Schleifenbaum H, Heidrich S et al (2011) High power selective laser melting (HP SLM) of aluminum parts. Phys Procedia 12:271–278. https://doi.org/10.1016/j.phpro.2011.03.035

46. Bean GE, Witkin DB, McLouth TD et al (2018) Effect of laser focus shift on surface quality and density of Inconel 718 parts produced via selective laser melting. Addit Manuf 22:207–215. https://doi.org/10.1016/j.addma.2018.04.024

47. Metelkova J, Kinds Y, Kempen K et al (2018) On the influence of laser defocusing in Selective Laser Melting of 316L. Addit Manuf 23:161–169. https://doi.org/10.1016/j.addma.2018.08.006

48. Qi T, Zhu H, Zhang H et al (2017) Selective laser melting of Al7050 powder: Melting mode transition and comparison of the characteristics between the keyhole and conduction mode. Mater Des 135:257–266. https://doi.org/10.1016/j.matdes.2017.09.014

49. Zhang J, Song B, Wei Q et al (2019) A review of selective laser melting of aluminum alloys: Processing, microstructure, property and developing trends. J Mater Sci Technol 35:270–284. https://doi.org/10.1016/j.jmst.2018.09.004

50. Kühn G (1986) W. Kurz, D. J. Fisher, Fundamentals of Solidification. Trans Tech Publications, Switzerland-Germany-UK-USA, 1986, ISBN 0-87849-523-3. Cryst Res Technol 21:1176–1176. https://doi.org/10.1002/crat.2170210909

51. Yang KV, Shi Y, Palm F et al (2018) Columnar to equiaxed transition in Al-Mg(-Sc)-Zr alloys produced by selective laser melting. Scripta Mater 145:113–117. https://doi.org/10.1016/j.scriptamat.2017.10.021